Journal of Geophysical Research: Solid Earth

Frictional stability-permeability relationships for fractures in shales

Yi Fang[1] (iD), Derek Elsworth[1,2], Chaoyi Wang[1], Takuya Ishibashi[1,3] (iD), and Jeffrey P. Fitts[4]

[1]Department of Energy and Mineral Engineering, EMS Energy Institute, and G3 Center, Pennsylvania State University, University Park, Pennsylvania, USA, [2]Department of Geosciences, EMS Energy Institute, and G3 Center, Pennsylvania State University, University Park, Pennsylvania, USA, [3]Fukushima Renewable Energy Institute, National Institute of Advanced Industrial Science and Technology, Koriyama, Japan, [4]Department of Civil and Environmental Engineering, Princeton University, Princeton, New Jersey, USA

Abstract There is wide concern that fluid injection in the subsurface, such as for the stimulation of shale reservoirs or for geological CO_2 sequestration (GCS), has the potential to induce seismicity that may change reservoir permeability due to fault slip. However, the impact of induced seismicity on fracture permeability evolution remains unclear due to the spectrum of modes of fault reactivation (e.g., stable versus unstable). As seismicity is controlled by the frictional response of fractures, we explore friction-stability-permeability relationships through the concurrent measurement of frictional and hydraulic properties of artificial fractures in Green River shale (GRS) and Opalinus shale (OPS). We observe that carbonate-rich GRS shows higher frictional strength but weak neutral frictional stability. The GRS fracture permeability declines during shearing while an increased sliding velocity reduces the rate of permeability decline. By comparison, the phyllosilicate-rich OPS has lower friction and strong stability while the fracture permeability is reduced due to the swelling behavior that dominates over the shearing induced permeability reduction. Hence, we conclude that the friction-stability-permeability relationship of a fracture is largely controlled by mineral composition and that shale mineral compositions with strong frictional stability may be particularly subject to permanent permeability reduction during fluid infiltration.

1. Introduction

Large-scale fluid injection into the subsurface (e.g., shale reservoir stimulation, geological storage of CO_2, deep disposal of wastewater, and enhanced geothermal stimulation) [*Healy et al.*, 1968; *Raleigh et al.*, 1976; *Kanamori and Hauksson*, 1992; *Shapiro et al.*, 2006; *Majer et al.*, 2007; *Suckale*, 2009; *Ellsworth*, 2013; *Walsh and Zoback*, 2015; *Guglielmi et al.*, 2015] can generate overpressures and induce seismicity by reactivating preexisting faults and fractures that are widely distributed throughout the upper crust [*Anderson and Zoback*, 1982; *McGarr et al.*, 2002] (Figure 1). The key to the success of these activities relies on (1) type of induced seismicity (i.e., low-frequency and slow-energy release rate in the form of aseismic events or fast-slip and high-energy release rate seismic events) and (2) desired permeability evolution—such as increased permeability for energy recovery systems and retained low permeability for caprock sealing systems. Hence, it is of particular interest to evaluate the relationship between the mode of fault reactivation (i.e., induced fault slip, including both seismic and aseismic modes) and fracture permeability evolution.

The permeability of faults is known to change during shear deformation due to the rearrangement and destruction of bridging asperities [*Elsworth and Goodman*, 1986]. When shear deformation occurs on a fracture, permeability may increase due to significant dilation [*Barton et al.*, 1985; *Ishibashi et al.*, 2016] or decrease as a result of progressive formation of gouge [*Faoro et al.*, 2009]. During fracture shearing, the frictional strength of the fracture is affected by the state of true area of solid-solid contact between the displacing surfaces [*Dieterich*, 1978]. This contact relationship provides a potential physical explanation for the rate-and-state friction laws that can evaluate whether a fault fails stably (aseismically) at slow creep rates of long duration (order of 1–100 mm/yr) or unstably (seismically) at fast frictional sliding rates of short duration (order of 1 m/s) under certain boundary conditions [*Brune*, 1968; *Anderson et al.*, 1996; *Schmidt et al.*, 2005; *Peng and Gomberg*, 2010]. Fault movement is governed by the frictional behavior of the fault gouge within the fault. This frictional behavior is adequately defined by rate-and-state friction laws [*Dieterich*, 1978; *Ruina*, 1983; *Marone*, 1998; *Scholz*, 1998]. Friction measurements indicate that the frictional strength and stability of simulated fault gouges are a function of mineralogy. This relationship is due to the distinct
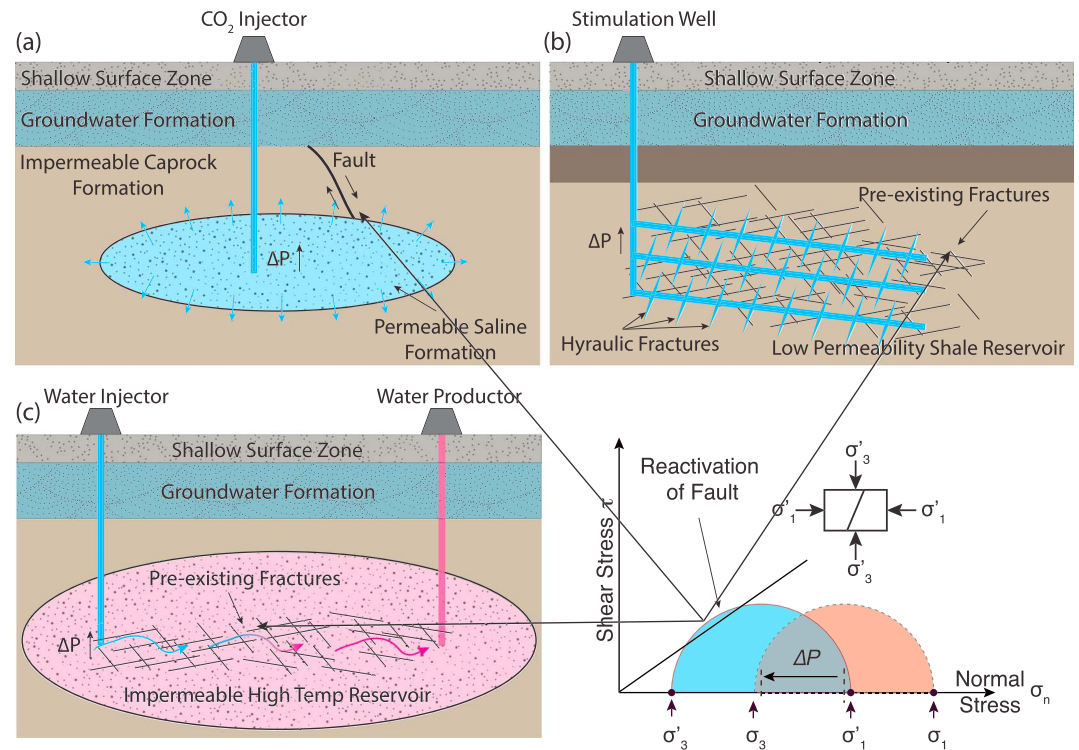
Figure 1. Schematic diagram illustrating three scenarios of fluid injection into the subsurface. (a) Geological CO_2 sequestration: the preexisting fault is embedded in the caprock formation at the boundary of saline formation. (b) Hydraulic fracturing of shale reservoir: preexisting faults are stimulated. (c) Enhanced geothermal system: hydraulic shearing in low permeability volcanic rocks. The Coulomb-Mohr circle shows that overpressure may destabilize and reactivate the fault.

crystalline structure and mechanical properties (e.g., plasticity, brittleness, and ductility) [*Ikari et al.*, 2011; *Kohli and Zoback*, 2013; *Niemeijer and Collettini*, 2013; *Fang et al.*, 2016] of different minerals as well as their swelling characteristics [*Heidug and Wong*, 1996; *Xu and Pruess*, 2004; *Mazumder and Wolf*, 2008]. Clay minerals, such as kaolinite, montmorillorite, chlorite, illite, smectite, muscovite, and mixed layer phases react with water-based fluids, leading to various degrees of swelling, dispersion, and migration characteristics [*Mohan et al.*, 1993; *Amorim et al.*, 2007]. Smectite and mixed layer clays exhibit crystalline swelling and hydration properties in an aqueous environment and experience significant volume expansion, which reduces the porosity and permeability of rocks [*Norrish*, 1954; *Norrish and Quirk*, 1954; *Young and Smith*, 2000]. Nonswelling clays, such as kaolinite and illite have less interaction with water than those of swelling clays, can easily disperse and migrate and lead to permeability damage [*Dodd et al.*, 1955]. At grain scale, with the effect of elevated temperature, stress-induced chemical dissolution of contacting asperities minerals may also change the contact area and alter the fracture conductivity [*Yasuhara et al.*, 2004, 2006; *Zhong et al.*, 2016]. A microphysical model has explained a competition between shear-induced dilatation and compaction via pressure solution transfer processes with respect to frictional stability in a simulated fault gouge [*Niemeijer and Spiers*, 2007]. These studies provide valuable insights into the formation-specific rheological response of fractures to deformation as seismic or aseismic—with implications for whether permeability evolution will be associated with these modes. Notwithstanding, it is still unclear whether there are different styles of permeability evolution for different frictional responses and whether the different styles can be inferred or predicted based on formation mineralogy.

In this study, we explore the possible link between frictional stability and the evolution of fracture permeability under upper crustal conditions where mineral reactions and thermally activated deformation mechanisms are too slow to be relevant (with the exception of clay swelling). We select two mineralogically distinct shale samples: Green River shale and Opalinus shale to perform frictional-permeability experiments, static non-shearing hydraulic tests, and imaging by X-ray computed tomography (CT) of both shale samples to probe
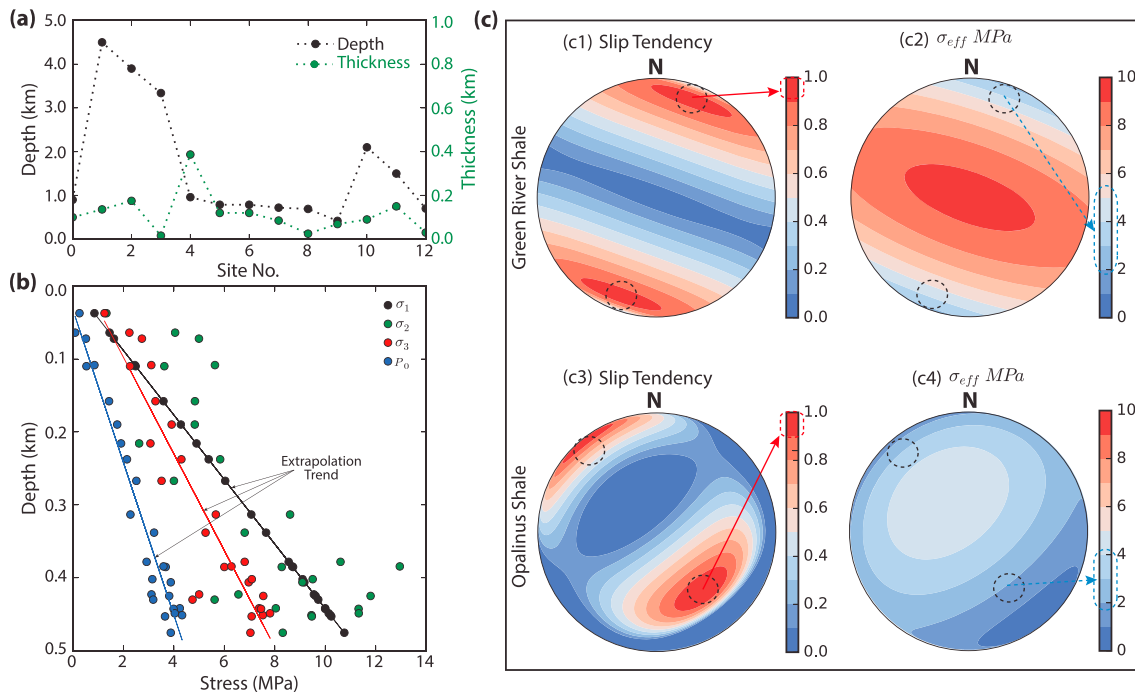
Figure 2. (a) Depth and thickness of shale reservoirs (data adopted from the report by *Allis et al.* [2001]). (b) In situ stress field of Green River Formation, Piceance Basin, Colorado (data adopted from hydraulic fracturing experiments by *Bredehoeft and Shuter* [1976]). (c) Lower stereographic projection of slip tendency and effective normal stress of fractures with required overpressure $\Delta P_f = 3.2$ MPa at the bottom (~950 m) of (c1 and c2) Green River Formation, Colorado and with required overpressure $\Delta P_f = 1.70$ MPa at the depth of ~ 270 m of (c3 and c4) Opalinus shale [*Corkum and Martin*, 2007].

the following key questions: (1) What is the fracture friction-permeability interaction that may occur during shear slip? (2) What is the influence of mineral composition of shale samples on friction and permeability behavior? And (3) what are the engineering implications of the friction-permeability relationships to activities such as caprock selection and pressure management for CO_2 geologic storage?

2. Experimental Methods

From the foregoing, it is clear that many parameters influence friction-permeability relationships, so it is important to capture the most critical factors at all scales. Thus, we first define key features that capture the most fundamental characteristics that influence permeability evolution during aseismic or seismic events and how these might be captured in experiments. We then introduce sample materials and preparation methods and finally define the experimental setup and procedures.

2.1. Assumptions and Conditions

To capture the key features of permeability-slip coupling, we list the following assumptions:

1. The preexisting fault is assumed to be a parallel plate model in the experiment and the cubic law is assumed to be valid for the fluid flow within the fracture. Although this model differs from a natural fracture with complex geometric surfaces, it provides the essential link between aperture and fluid transmission rate [*Snow*, 1969] and is consistent with the geometry of fracture slip [*Dieterich*, 1992].

2. The normal stress applied in the experiment is equivalent to the in situ effective normal stress that acts on the most favorably orientated fractures after an overpressure is applied. Considering the shallow depths of shale reservoirs [*Allis et al.*, 2001], we assume that the local effective normal stress on the surface of a shale fracture is relatively low (Figure 2a), so the effective normal stress used in the experiments might be comparable to some potential GCS reservoirs. However, for reliable extrapolation to deeper GCS fields, we need a microphysical model accommodating the effects of temperature and effective normal stress.

3. The applied experimental loading velocity (10^0 μm/s to 10^1 μm/s) does not purport to cover the full spectrum of possible seismic or aseismic transient slip velocities but represents a narrow range where
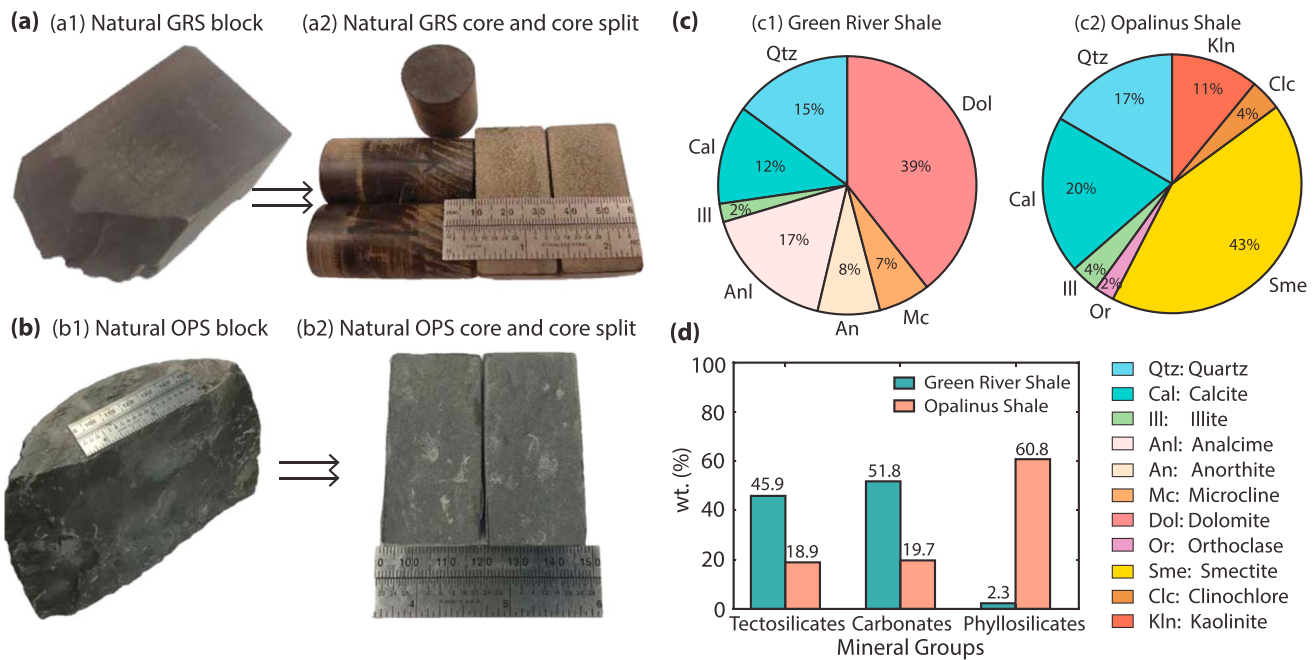
Figure 3. (a) Natural (intact) Green River shale block and cores and saw cut half split of the cores. (b) Natural (intact) Opalinus shale block and cores and saw cut half split of the cores. (c) XRD analysis of mineral compositions of both Green River shale and Opalinus shale. (d) Comparison of mineral groups (tectosilicate, carbonate, and phyllosilicate) between Green River shale and Opalinus shale.

contrasting responses of different mineralogies may be explored, with velocity as a control parameter. As the sliding velocity in these experiments is approximately 2 orders of magnitude lower than similar experiments, no thermal pressurization effect is considered [*Rice*, 2006; *Tanikawa et al.*, 2010, 2014].

2.2. Sample Materials and Preparation

In this experiment, we select two natural shales with distinctly mineralogy—Green River shale and Opalinus shale. Green River shale is deposited in a fresh water lacustrine environment. The samples are recovered from the sequence at Grand Junction, Colorado. The in situ stress field of the Green River Formation [*Bredehoeft and Shuter*, 1976] suggests a strike slip faulting regime near the surface and a normal faulting stress regime below a depth of ~200 m (Figure 2b), with the maximum horizontal stress σ_H trending N70°W. Stratigraphic analysis indicates that the base of the Green River shale formation is at a depth of ~950 m [*Dyni*, 2006]. Thus, from the measured stress gradient in Figure 2b, local in situ stresses and fluid pressures are estimated as $\sigma_v = 21.5$ MPa, $\sigma_H = 20.0$ MPa, $\sigma_h = 14.9$ MPa and $P_0 = 8.8$ MPa, respectively. The Opalinus shale is clay-rich shale (Figure 3d) and is representative of caprock materials for a large number of reservoirs targeted for carbon dioxide storage. The Opalinus core sample is taken from a horizontal borehole (BEZ-G50) at the Mont Terri underground rock laboratory in Switzerland, where the in situ stresses are $\sigma_v = 6.5$ MPa, $\sigma_H = 4.0$ MPa, $\sigma_h = 2.2$ MPa, $P_0 = 1.7$ MPa, and a fracture cohesion $C_f = 1.0$ MPa [*Corkum and Martin*, 2007].

For the experiments, cores with longitudinal lengths of 5 cm and diameters of 2.5 cm are drilled and carefully saw cut and polished into two halves, representing a parallel plate model (Figures 3a and 3b). The planar surfaces are uniformly roughened with grinding powder (#60 Grit) at constant rate. The mineralogical composition of the samples was characterized via X-ray diffraction, suggesting that Green River shale (GRS) is carbonate rich with an equivalent proportion of tectosilicate while Opalinus shale (OPS) is primarily composed of phyllosilicates (Figures 3c and 3d).

2.3. Experimental Setup and Procedure
2.3.1. Friction-Permeability Experiments

The friction-permeability experiments were performed in a triaxial testing apparatus that independently applies confining pressure and differential (end-to-end) pore pressure while the sample is sheared at a prescribed velocity. This allows the concurrent measurement of the evolution of fracture permeability and
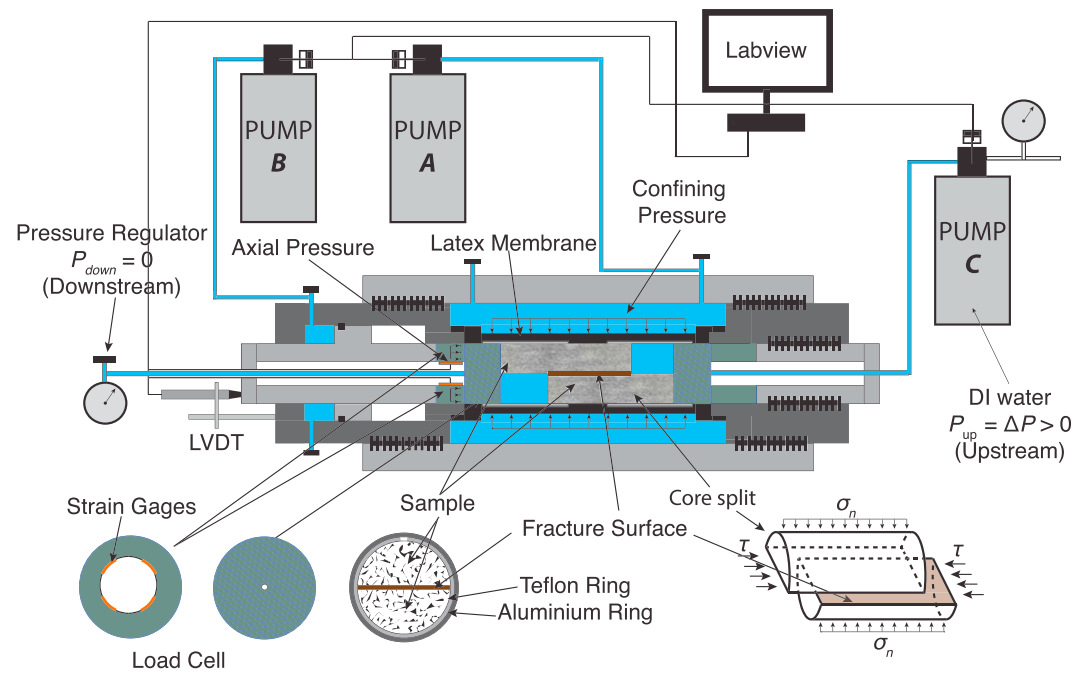
Figure 4. Picture of experimental setup for friction-permeability evolution test: Pump A (ISCO500D) controls the confining pressure (normal stress) applied on the fracture. Pump B (ISCO500D) controls pressure that provides the source of shear stress applied on the fracture. Pump C (ISCO500D) injects the fluid at a prescribed flow rate or pressure, allowing the fluid source locates at the origin of the fracture and flow along the fractures.

friction (Figure 4). The reassembled split samples were packed within a latex membrane with an initial offset of 10 mm for slip displacement during sliding. An aluminum ring is placed at 10 mm offset to prevent fluid extruding. To reduce the friction between the outer wall of the sample, aluminum ring and the membrane, we wrapped the sample in Teflon tape.

From the estimated in situ stresses in section 2.2, the equivalent effective normal stresses at which critically stressed fractures will fail range from 2 MPa to 5 MPa (Figure 2c). Thus, we apply a confining stress (normal stress) of 3 MPa (pump A) and set a constant upstream fluid pressure (pump C) during axial shear displacement at constant rate (pump B) and measured force. The minimum flow rate of each pump is 0.001 ml/min and the display resolution of the pump pressure transducer is 1.0 kPa. A load cell with a resolution of 0.3 kPa is used to measure the axial stress. At room temperature, the minimum measurable transient fracture permeability is 1.0×10^{-14} m^2.

We conducted both constant velocity and velocity-stepping experiments to compare the hydraulic behavior response to varying velocities. For the Green River shale, the shear velocity was set to 1 μm/s (monotonic) and switched by upsteps and downsteps between 1 μm/s and 10 μm/s, until a displacement of ~10 mm was reached. These conditions were repeated for Opalinus shale, but with an initial shear velocity at 10 μm/s to minimize the competing time-dependent swelling effect of clay minerals, with upsteps and downsteps completed (1 μm/s and 10 μm/s) to a final shear offset of ~8 mm. All the experiments were performed at room temperature (25°C), with shear displacements recorded by LVDT (Linear Variable Differential Transformer) located outside the vessel.

2.3.2. Static Nonshearing Hydraulic Experiments
The X-ray diffraction (XRD) analysis (Figure 3) of both the Green River and Opalinus shales show that Green River shale is carbonate rich and is assumed to be more brittle while the Opalinus shale is clay dominated and shows ductile macroswelling behavior during excavation [*Bossart et al.*, 2004]. Due to the inhomogeneity of the shale samples from the sedimentation processes, mineral phase contents of these shale samples are variously reported [*Wenk et al.*, 2008; *Kaufhold et al.*, 2013].

To examine the swelling effect and to isolate its influence on the permeability from the shearing response, we measure permeability under the same uniform stress as before but for null shearing velocity in the sample
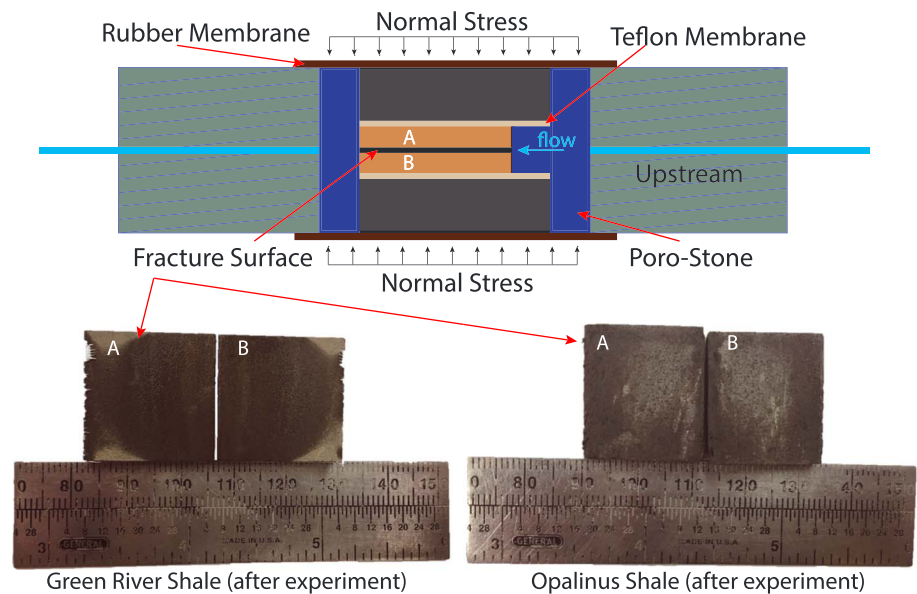
Figure 5. Experimental configuration and sample geometry for static nonshearing hydraulic experiments for both Green River shale and Opalinus shale.

configuration of Figure 5. We apply identical initial fracture roughness to both samples. The initial upstream pressure of 0.01 MPa is incrementally increased when the flow rate reaches steady state. For Opalinus shale, we directly apply an initial hydraulic pressure at 0.5 MPa to ensure fluid migration through the fracture at the first hydraulic pressure step. The detailed hydraulic pressure and flow rate results of both samples are illustrated in Figure 7.

2.3.3. Tomographic Imaging

Samples are characterized by white light optical profilometry and 3-D X-ray imaging to (1) control and ensure that the statistical fracture roughness before the friction-permeability and static nonshearing experiments are of the same magnitude; (2) measure the evolved fracture roughness after the experiments; (3) observe the wear products generated during the experiments at analogous in situ conditions; and (4) monitor the short-term swelling effect of the clay-rich Opalinus shale fracture under wetting.

White light interferometry was performed using a Zygo NewView 7300 with a 10X objective (Figure 6a), and data were processed with Mx^{TM} software (Zygo). The root-mean-square (RMS) asperity height is characterized on the sample fields of 1.66 mm × 1.66 mm as an index of fracture surface roughness of both Green River and Opalinus samples both before and after the friction-permeability and static nonshearing experiments (Figure 6c).

To capture the features of the wear products that are generated during sliding, we first manually inject Canada balsam (diluted by 40% ethyl alcohol) by syringe to freeze the state of the fracture immediately after the sliding experiment with the normal stress unchanged. We then apply X-ray computed tomography (xCT) to produce 3-D images of fracture contacts. We also use xCT in rapid data collection mode to observe the temporal evolution of swelling in response to aqueous fluid flow within fractures of the clay-rich Opalinus shale. The Green River shale subcore is scanned at standard mode (~12 min/scan) with larger voxel dimension. On the contrary, to avoid the effect of time-dependent water evaporation during the wetting process for the Opalinus shale, we use a rapid scanning mode (~1.5 min/scan) to observe the swelling behavior of Opalinus shale. X-ray tomography data were collected on the bending magnet beamline 13BMD at the GeoSoilEnviroCARS sector 13 of the Advanced Photon Source (APS), Argonne National Laboratory (ANL), Illinois, USA (Figures 6b and 6d). Tomograms were obtained with a monochromatic X-ray beam (34.5 keV), sample rotation scheme, and downstream scintillator, focusing optics and CCD detector combination that produced reconstructed 3-D images with a 2.88 μm voxel dimension. See *Gualda and Rivers* [2006] for detailed descriptions of data collection and processing methods.
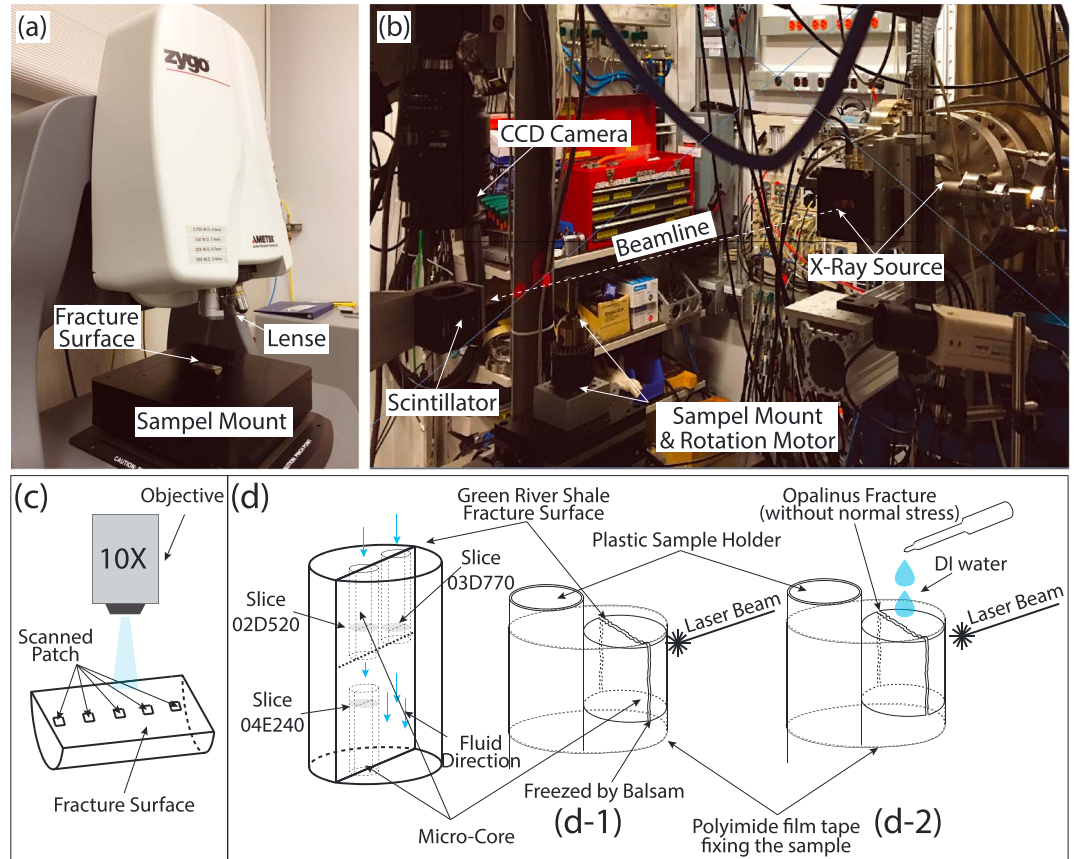
Figure 6. (a) Three-dimensional optical surface profiler for characterizing statistical roughness of fracture surface. (b) APS GSECARS Beamline 13BMD Experimental Setup for characterizing the fracture asperity contacts at postmortem conditions. (c) Fracture surface for white light scanning. (d-1) Microcores of Green River shale for xCT imaging. (d-2) Opalinus shale fracture with DI water for xCT imaging.

3. Results and Discussion

We interpret measurements of concurrent flow and deformation to recover friction-stability-permeability evolution in the context of rate-state friction models. This analysis consists of (1) rate-and-state friction response to calculate the frictional parameters from measured data, (2) cubic law representation to estimate permeability, and (3) parametric stress and slip-dependent aperture analysis that reveals the mechanism of evolving permeability. Additionally, we perform an analysis of the permeability evolution measured by the static nonsheared hydraulic experiments and tomographic characterizations, in order to segregate and interpret the swelling behavior and its effect on the friction-permeability relationship.

3.1. Data Analysis

We calculate the coefficient of friction μ as a function of shear displacement using $\mu = \tau/\sigma_n$, ignoring cohesion. The velocity dependence of friction can be interpreted in the framework of rate-and-state friction (RSF) theory [*Dieterich*, 1978, 1979; *Ruina*, 1983]. In the RSF approach to modeling fracture shear slip, the friction coefficient is written as [*Dieterich*, 1978; *Marone*, 1997; *Scholz*, 1998]

$$\mu(V, \theta) = \mu^i + a \ln\left(\frac{V^i}{V^{i-1}}\right) + b \ln\left(\frac{V^{i-1}\theta^i}{D_c^i}\right) \tag{1}$$

$$\frac{\mathrm{d}\theta^i}{\mathrm{d}t} = 1 - \frac{V^i\theta^i}{D_c^i} \tag{2}$$

where μ_0 is the coefficient of friction at a reference velocity V^{i-1}; θ^i is a state variable that evolves after the velocity is incremented (stepped up or down) to V^i; a and b are the friction parameters which represent

the direct effect (*a*) and the evolutionary effect due to a step velocity change (*b*); and D^i_c is the critical slip distance, over which evolution to a new steady state takes place. Frictional slip instability is determined in part by the parameter (*a-b*) derived from equation (1) for a finite step in velocity, yielding [*Dieterich*, 1979; *Ruina*, 1983; *Scholz*, 1998]

$$a - b = \frac{\left(\mu^i_{ss} - \mu^{i-1}_{ss}\right)}{\ln\left(V^i/V^{i-1}\right)} \tag{3}$$

A positive value of (*a-b*) denotes velocity-strengthening behavior, suggesting stable, aseismic slip, while a negative (*a-b*) indicates velocity-weakening behavior, which is potentially unstable. The RSF constitutive parameters were determined by fitting experimental and modeled data via equations (1) and (2).

The measured fracture permeability k_m (m^2) can be expressed in terms of measured hydraulic aperture b_m (m) based on the cubic law

$$bm = -\left(\frac{12\mu_{vis} \cdot L(t) \cdot Q(t)}{W \cdot \Delta P_f}\right)^{1/3} \quad \text{and} \quad k_m = \frac{b^2_m}{12} \tag{4}$$

where μ_{vis} (Pa s) is the viscosity of fluid; $L(t)$ (m) is the contact length of the fracture surface; W (m) is the fracture width; $Q(t)$ (m^3/s) is the measured flow rate and ΔP_f (Pa) is the differential pressure between the upstream and downstream extent of the fracture.

Elastic and plastic deformations of asperity contacts are the key physical processes to interpret the frictional evolution during sliding [*Rabinowicz*, 1951; *Yoshioka and Scholz*, 1989; *Wang and Scholz*, 1994; *Yoshioka*, 1997; *Misra*, 2002]. Correspondingly, fracture permeability is governed by the evolution of fracture aperture that is mainly stress dependent. In the laboratory, the aperture distribution of a fracture at laboratory scale (10^{-2} m to 10^0 m) can be determined by measuring the asperity heights of a fracture [*Brown and Scholz*, 1985]. Here we define a constitutive aperture model that describes the relationship between friction and permeability considering the effects of both shear slip displacement and velocity change. Before the preexisting fracture is reactivated, the fracture aperture may be expressed as a nonlinear normal stress-dependent b_0 [*Rutqvist et al.*, 2004]

$$b_0 = b_r + (b_{max} - b_r) \ \exp[-\alpha_n \ (\sigma_n - p_f)] \tag{5}$$

where b_r (m) is the residual hydraulic aperture; b_{max} (m) is the maximum opening; α_n (1/MPa) is the normal stiffness parameter determined from experiments; σ_n (MPa) is the normal stress perpendicular to the fracture surface; and P_f (MPa) is the internal fluid pressure in the fracture. After the reactivation of a preexisting fracture, the shear slip-dependent aperture b_{slip} (m) may be empirically defined as

$$b^i_{slip} = b_f + (b_{s0} - b_f) \ \exp\left[-\alpha_s \cdot \frac{u(V^i, t)}{L_0} \cdot \mu(V^i, \theta^i) \cdot (\alpha_n - P_f)\right] \tag{6}$$

where the index *i* refers to the *i*th velocity step (if the velocity is constant throughout the shear slip, *i* = 0); b_f (m) is the final aperture after sufficient shear displacement to reach steady state; b_{s0} (m) is the initial shear slip aperture; α_s (1/MPa) is the shear stiffness parameter; $u(V^i,t)$ (m) is the shear displacement as a function of sliding velocity and time; L_0 (m) is the contact length of the fracture surface before shear slip; and $\mu(V^i, \theta^i)$ is the concurrently measured frictional strength.

Analogous to the shear dilation relationship of *Samuelson et al.*, 2009, we define a dilation or compaction parameter $\Delta\phi^i$ to represent the volumetric response after failure as

$$\Delta\phi^i = \frac{\Delta b^i_{vel}}{b^{i-1}_{slip}} = \psi^i \cdot \ln\left(\frac{V^{i-1}}{V^i}\left[1 + \left(\frac{V^i}{V^{i-1}} - 1\right) \cdot e^{-Vi \cdot ti/D^i_c}\right]\right) \tag{7}$$

where Δb^i_{vel} (m) is the aperture change due to the *i*th velocity change in the slip history; b^{i-1}_{slip} (m) is the aperture at the moment before the shear velocity is stepped; ψ^j is a compaction/dilation factor that pertains to the fracture material and generated wear products; t^i (s) is the time since the *i*th velocity step. Hence, the modeled fracture aperture b_{evo} (m) that evolves during shear slip and the corresponding permeability k_f (m^2) are expressed as

$$b_{evo} = b^{i-1}_{slip}(1 + \Delta\phi^i) \quad \text{and} \quad k_f = \frac{b^2_{evo}}{12} \tag{8}$$
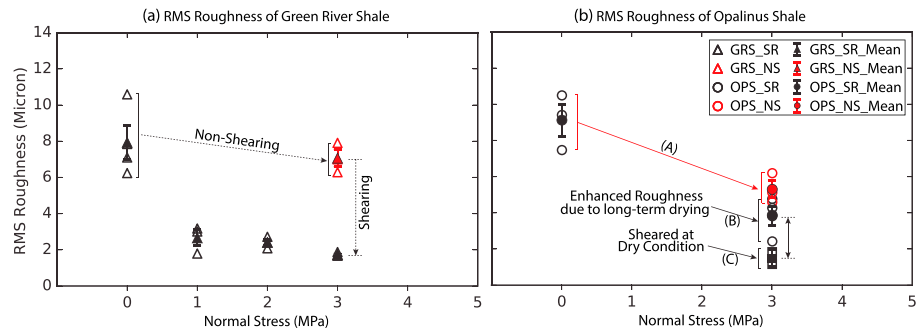
Figure 7. Root-mean-square (RMS) roughness of planar fracture surface of a split core of (a) Green River shale and (b) Opalinus shale. Plots with normal stress at 0 refer to the initial asperity before shear sliding. Plots with normal stress at 1 to 3 MPa refer to the asperity after shear sliding (SR stands for the sheared experiments). Plots in red at 3 MPa refer to static nonshearing hydraulic experiments (NS refers to nonshearing). In Figure 7b, the black squares refer to friction experiments at dry condition. Arrow (A) refers to the reduced roughness by swelling in a nonshearing experiment. Arrow (B) refers to the roughness value when fracture is sheared at wet condition. Due to the long-term drying, the measured roughness value is higher than its real value when the shearing was just finished. Arrow (C) refers to roughness value of fracture sheared at dry condition.

3.2. Analysis of Measured Data

3.2.1. Friction-Permeability Relationship

Asperity damage is manifested as a change in roughness of the fracture surface. In Figure 7, the root-mean-square (RMS) asperity height of a monotonically sheared fracture of Green River shale (black triangles at 1 to 3 MPa) and Opalinus shale (black circles and squares at 3 MPa) are significantly reduced due to the shearing and increased normal stress, suggesting that the surface roughness evolves by progressive removal of the highest asperities from the surface.

The frictional constitutive parameters of Green River shale and Opalinus shale are listed in Table 1. The average friction coefficient value of Green River shale ($\mu = 0.573$) is larger than that of Opalinus shale ($\mu = 0.502$). The experimental slip displacement is at the same scale of displacement (e.g., 0.1 mm to 10 mm) in microearthquakes ($M_w < 2.5$) or aseismic slip events [*Zoback and Gorelick*, 2012; *Guglielmi et al.*, 2015]. The (a-b) value of Green River shale decreases with displacement from 0.0027 to 0.0022 with an average value of 0.0025, showing a slight velocity strengthening when the velocity step is applied. The (a-b) value of Opalinus shale decreases with displacement from 0.0155 to 0.0140 with an average value of 0.0152, suggesting a much stronger velocity-strengthening behavior than that of Green River shale under same experimental conditions. This implies that fractures in Opalinus shale tend to fail aseismically at low effective normal stresses congruent with rate-and-state friction theory.

Table 1. Friction Experiment Data Summary

| Sample	Normal Stress (MPa)	Velocity Step	Velocity (µm/s)	Friction Coefficient	(a-b)	D_c (µm)
Green River	3	1	1 to 10	0.576	0.0027	600
		2	10 to 1	0.578	0.0026	500
		3	1 to 10	0.565	0.0022	500
Average[a]				0.573	0.0025	533
Opalinus	3	1	10 to 1	0.569	0.0155	370
		2	1 to 10	0.521	0.0152	430
		3	10 to 1	0.532	0.0173	360
		4	1 to 10	0.466	0.0149	460
		5	10 to 1	0.482	0.0146	330
		6	1 to 10	0.442	0.0140	440
Average[a]				0.502	0.0152	398
Green River	3	Constant[b]	1	0.571	-	-
Opalinus	3	Constant[b]	1	0.498	-	-

[a]The average value of friction coefficient and (a-b) values are obtained from averaging the results of all velocity steps.
[b]The friction coefficients of GRS and OPS at constant velocity are evaluated by averaging the friction values after the frictional peak.
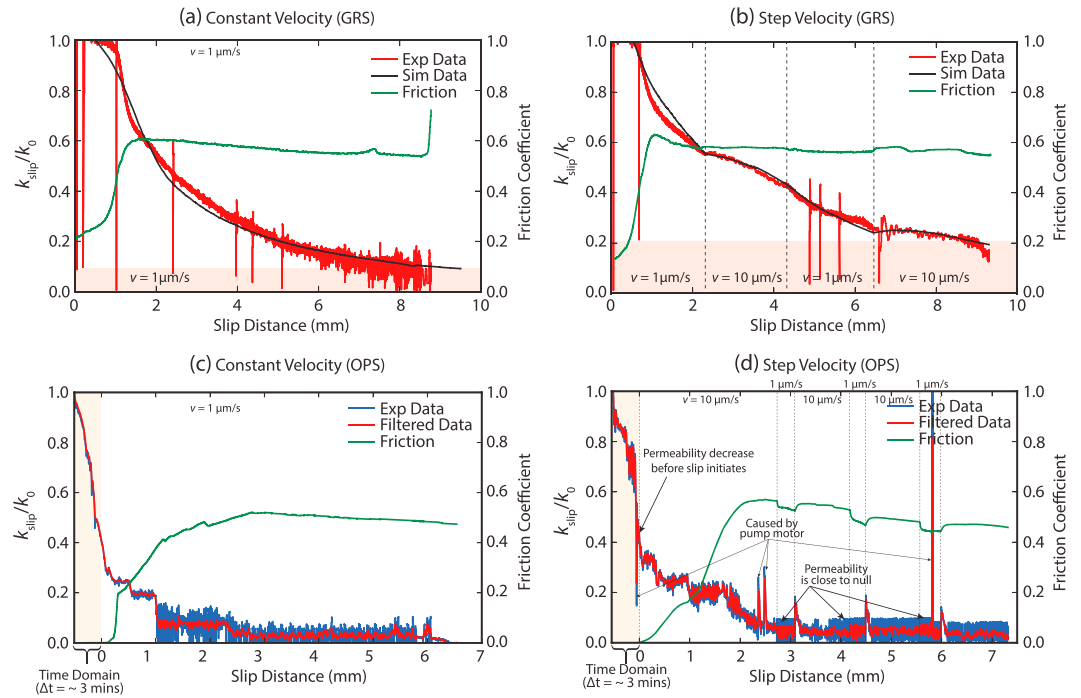
Figure 8. Diagrams showing relationship between measured friction (green curve), measured permeability (red curve), and sliding velocity (constant versus stepped velocity) for Green River shale (GRS) and Opalinus shale (OPS). Simulated permeability is shown in black. (a) Scenario of constant slip velocity (1 µm/s) for GRS with initial permeability k_0 of 82.302×10^{-12} m^2. (b) Scenario of stepped slip velocity (1 µm/s, 10 µm/s, 1 µm/s, and 10 µm/s) for GRS with k_0 of 74.332×10^{-12} m^2. The shaded area at the bottom of both diagrams highlight final permeability magnitude after shearing. (c) Scenario of constant slip velocity (1 µm/s) for OPS with k_0 of 7.301×10^{-12} m^2. (d) Scenario of stepped slip velocity (10 µm/s, 1 µm/s, 10 µm/s, 1 µm/s, 10 µm/s, and 1 µm/s) for OPS with k_0 of 8.801×10^{-12} m^2.

For the case of Green River shale, the impact of asperity reduction is reflected in Figures 8a and 8b, where the frictional strength (green curve) decreases slightly after reaching a peak and stabilizes within the range of ~0.57 to ~0.59 at a slip distance of ~8 mm. The removed asperities contribute to the generation of wear products of various particle sizes. The largest (with diameter size > ~10 µm) are captured in the xCT images while the smaller ones are removed from the sample with the impregnation by the highly viscous Canada balsam (Figure 9). In addition, the reconfigured asperities change the hydraulic properties of Green River shale as illustrated in Figures 8a and 8b (red curve). The measured permeability declines exponentially at a constant sliding velocity (Figure 8a). Although Figure 8b shows a similar declining trend of the measured
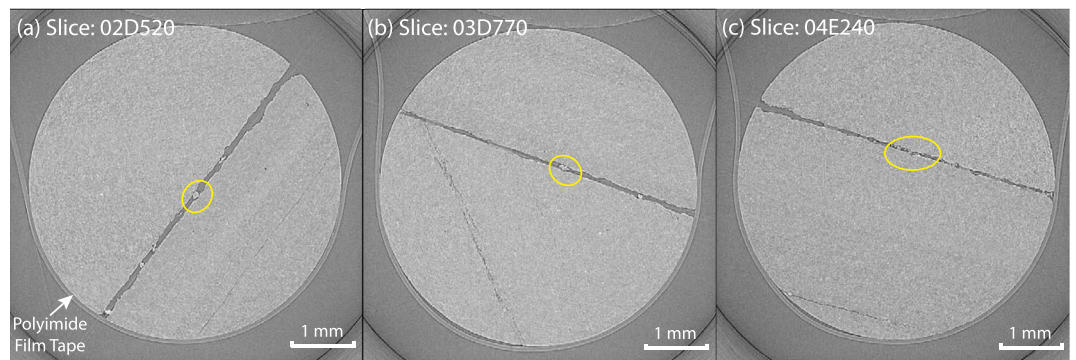
Figure 9. Subcores of Green River shale fracture (see Figure 6d) for the xCT experiments. The fracture is filled with Canada balsam. (a) The xCT image from subcore 02. (c) The xCT image from subcore 03. (d) The xCT image from subcore 04. Yellow circles locate the large particles (wear product generated during shearing).

permeability, the change in sliding velocity from 1 to 10 μm/s clearly slows down the rate of permeability decrease. Conversely, when the sliding velocity drops from 10 to 1 μm/s, the rate of permeability decrease accelerates. Clearly, after a shear slip of 6 to 8 mm, the slope of the decrease in permeability flattens, suggesting that the asperity height distribution experienced a relatively small change. It is noteworthy that the eventual permeability for the up-stepped velocity is enhanced by ~10% compared to that at constant velocity. This implies that a high velocity may, to some extent, enhance fracture permeability.

To yield a better understanding of the mechanisms of permeability evolution, we represent the permeability evolution using equations (5) to (8) and show the results (black curve) in Figures 8a and 8b. The parameters adopted in the model are listed in Table 2. The modeled permeability matches well with the measured permeability for both constant velocity and stepped velocities. These results may be interpreted as follows: (1) within the slow slip velocity domain, permeability always declines as shear slip increases due to the reduction of asperity height up to the time that a steady state asperity height is reached; (2) with the generated wear products embedded within the two fracture walls, changing the sliding velocity may enhance or diminish the rate of change of permeability via dilation or by compaction. Thus, comminution will favor a reduction in permeability, by reducing pore-throat size, and dilation in the absence of comminution will favor permeability increase.

For the case of Opalinus shale, though the trends of friction and permeability evolution of Figures 8c and 8d are similar to those of Green River shale, we do observe some differences in their hydraulic and frictional behaviors. First, there is significant damage (reduction in permeability) during the first ~3 min before the initiation of shear slip for both constant velocity and stepped velocity. When the permeability reduced to ~35% of its initial magnitude, shear slip was started at a sliding velocity of 10 μm/s. The declining rate of permeability starts increasing until the frictional strength curve becomes flat at a sliding displacement of ~1.8 mm. When the frictional strength reaches steady state (~0.55), at a sliding displacement of ~2.7 mm, the permeability drops to a stable level (equal to approximately null). In contrast with the velocity-stepped permeability evolution of the Green River shale (Figure 8b), the permeability change of the Opalinus shale is smaller than the measurement error at these low permeabilities. This implies that friction and permeability are decoupled if the fracture is fully sealed with swelling clay-rich particles. In terms of frictional stability, the strong strengthening behavior is the result of clay-rich materials that may promote swelling during fluid infiltration. Correspondingly, we postulate that strong frictional stability may result in permeability destruction.

The experimental results are broadly honored by the model (Figures 8a and 8b). From equations (5) to (8), geomechanical controls can be attributed to both normal and shear stress effects on the fracture aperture and asperities, which define the hydraulic behavior of the fractures. To understand how sensitive the permeability evolution of fractures is to these parameters, and the potential effects of these sensitivities on the interpretation of the measured data, we perform a parametric study to isolate the individual effect of each parameter from the ensemble of integrated effects. In the model, the velocity step is applied at a displacement of 4 mm, before which wear products and friction are assumed to reach steady state.

Individually, in Figure 10a higher D_c values (critical slip distance) result in a smooth change of permeability, due to the fracture

Table 2. Parameters Used in Permeability Modeling in Figure 8[a]

Parameters	Symbol	Value	Units
Residual hydraulic aperture	b_r	1.0e−5	m
Maximum aperture	b_{max}	2.2e−5	m
Final aperture after shear	b_f	2.5e−6	m
Critical slip distance	D_c^i	600, 500, 500	μm
Loading velocity	V^i	1, 10, 1, 10	μm/s
Compaction/dilation factor	ψ^i	0.09, 0.03, 0.09	-
Effective normal stress	σ_{neff}	3.0	MPa
Initial contact length	L_0	18.8	mm
Nonlinear normal stiffness	α_n	0.3	1/MPa
Nonlinear shear stiffness	α_s	0.064	1/MPa

[a]Loading velocity V^i and effective normal stress σ_{neff} are applied experimental conditions. Critical slip distance D_c^i can be estimated by frictional experiments. Residual hydraulic aperture b_r, maximum aperture b_{max}, and final aperture b_f after shearing can be measured using surface characterization method as illustrated in Figure 6c. Nonlinear normal stiffness α_n and nonlinear shear stiffness α_s are empirical parameters that can be estimated by the curvature of aperture-normal/shear stress function in normal and shear deformation experiments [*Davies and Davies*, 2001; *Rutqvist et al.*, 2002]. Initial contact length L_0 is known in initial experimental setup. Compaction/dilation factor ψ^i is an estimated fitting parameter.
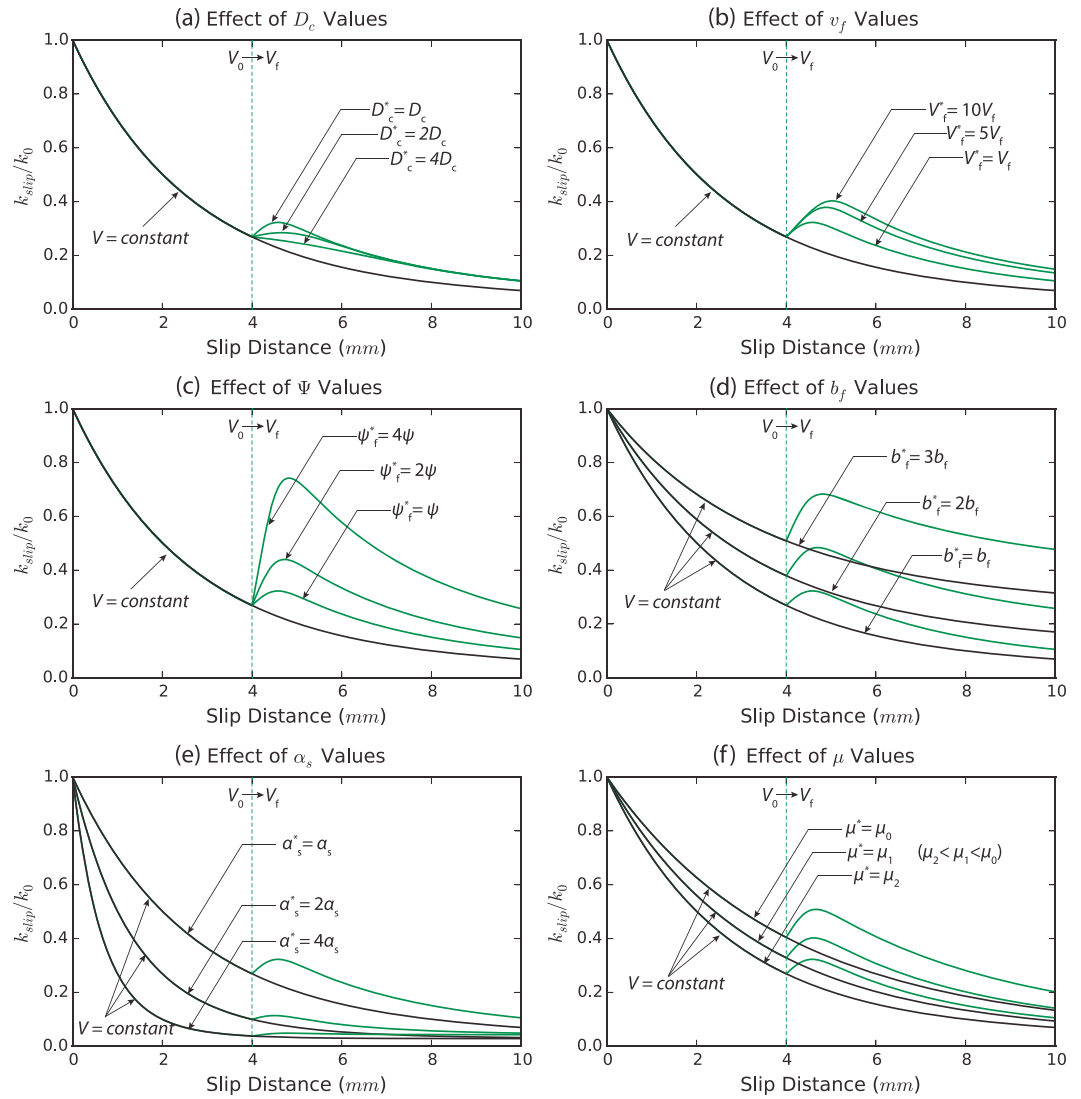
Figure 10. Parametric analysis: (a) Effect of critical displacement (D_c). (b) Effect of velocity upstep (V_f). (c) Effect of dilation or compaction parameter (ψ). (d) Effect of reduced final aperture (b_f). (e) Effect of shear stiffness parameter (α_s). (f) Effect of frictional strength (μ). The black curves show the permeability evolution under constant velocity shearing while the green curves represent the permeability change after a velocity step applied. Model reference case parameters in each plot ($D^*_c = D_c$, $V^*_f = V_f$, $\psi^* = \psi$, $b^*_f = b_f$, $\alpha^*_s = \alpha_s$, $\mu^* = \mu$) are referred from experimental values.

asperities taking longer to reconcile and relocate relative to each other. Increasing the velocity will inevitably enhance the dilation effects (if the dilation parameter ψ is positive) (Figure 10b). However, this enhancement asymptotes to an upper limit when upstep velocity grows to infinity, indicating that the velocity change is only the trigger for the permeability change but not the dominant controlling process. In comparison, an increase of the dilation parameter (ψ) can significantly enhance the permeability after a velocity step occurs (Figure 10c). In Figure 10d, the reduced final aperture crucially determines the background permeability evolution where a large final aperture would result in a small permeability decrease. This behavior is largely controlled by the applied normal stress and the strength of the asperity where high normal stress and a weak asperity would result in a larger contact area of the fracture surfaces. Likewise, the shear stiffness parameter α_s determines how fast the asperities are destroyed during the shearing and controls the timing of the permeability reduction with slip distance (Figure 10e). For example, a higher shear stiffness parameter α_s suggest that the permeability declines faster to its steady state. The effect of frictional strength (μ) is illustrated in Figure 10f, indicating that high frictional strength leads to a smaller

permeability decline. As frictional strength is a function of mineral composition, where strong minerals resist deformation, this leads to a minimal decline in permeability.

Summarized from the above analysis, Figure 7 shows that critical displacement (D_c), incremented-velocity (V_f), and the dilation or compaction parameter (ψ) only play a role in influencing the permeability after a velocity change (Figures 10a–10c), while the influences of the final aperture (b_f), shear stiffness parameter (α_s), and frictional strength (μ) accompany the entire shearing process (Figures 10d–10f).

3.2.2. Effect of Swelling

The static nonshearing hydraulic experiments demonstrate that swelling plays a significant role in the friction-permeability relationship for the clay-rich Opalinus shale but only a negligible role for the carbonate-rich Green River shale. The flow rate through the fracture in Green River shale increases or decreases linearly with fluid pressure (Figure 11a). The fluid percolates through the fracture of Green River shale at a very low pressure (e.g., 0.01 MPa), while flow initiates only above 0.5 MPa for the Opalinus shale. At constant pressure, the flow rate within the Opalinus shale is reduced to only 6% of its initial rate within ~10 min and essentially stops (~0 ml/min) at ~120 min (Figure 11b) due to closure of the fracture by the swelling of clay minerals. A high fluid pressure (~1.5 MPa) is required to reopen the fracture. In Figure 11c, the permeability of the Green River shale remains constant for the first ~10 min and declines slightly when the fluid pressure is stepped to 0.06 MPa and eventually rebounds back to its initial magnitude after the fluid pressure drops to 0.01 MPa. In contrast, the permeability of the Opalinus shale drops permanently to a value sufficiently low (i.e., not resolvable by experimental setup) over the same time scale (~120 min), implying that permeability damage is occurring (Figures 8c and 8d) and is primarily a result of the swelling-induced sealing of the fracture.

A comparison of fracture roughness after the nonshearing hydraulic experiments is shown in Figure 7. It is observed that the roughness of the fracture in Green River shale reduces (red triangles at 3 MPa in Figure 7a) in comparison to its initial state (black triangles at 0 MPa). This may be due to the irreversible deformation of the asperities under the increased normal stress. However, the apparent roughness of the fracture in the Opalinus shale reduced markedly after the experiment (red circles at 3 MPa in Figure 7b) compared to before the experiment (black circles at 0 MPa). This decrease is likely a result of swelling and attendant flattening of the fracture surface (Figure 7b). It is worth noting that the roughness of the sheared
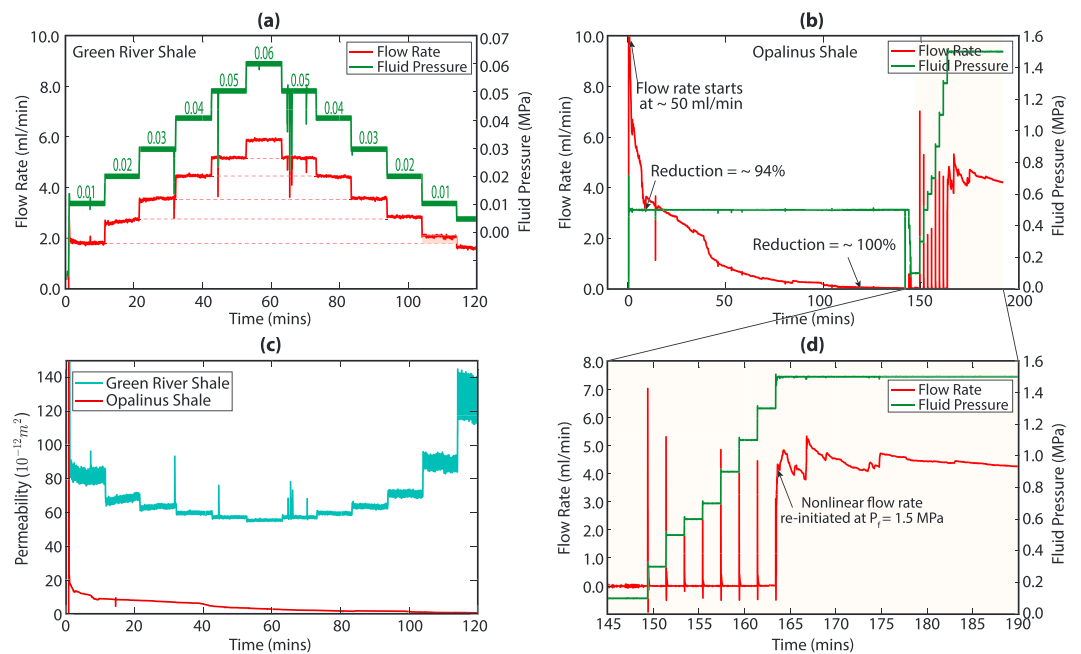
Figure 11. Results of static nonshearing hydraulic experiments of Green River shale and Opalinus shale. (a) Temporal evolution of gauge pressure and injected flow rate for Green River shale. (b) Temporal evolution of gauge pressure and injected flow rate for Opalinus shale. (c) Comparison of temporal evolution of permeability between Green River shale and Opalinus shale. (d) The pink shading highlights a condensed data section in Figure 11b.

Opalinus fracture surface (black circles at 3 MPa) is slightly enhanced due to drying for the unconstrained situation where the fracture is exposed to the air.

Furthermore, swelling-induced fracture sealing within the Opalinus shale was independently observed using time-dependent xCT imaging (Figure 12). The time sequence of xCT images shows that within a short time period after the wetting (<3 min), the shale matrix expansion is captured. The unconfined fractures begin to adhere to each other. After a period of 30 min, the partial fracture surfaces are filled with swelled minerals, demonstrating how swelling in clay-rich shales under confining pressure can result in fracture closure and permeability reduction. However, during this process, the swelling effect is gradually reduced due to the fast water evaporation.

3.3. Summary

These observed responses, can be summarized with a proposed conceptual model that considers three distinct modes of friction-stability-permeability evolution in a low effective normal stress regime (Figure 13). These different conditions include where (1) the fracture asperities are composed of strong-brittle minerals that are difficult to comminute into finer particles during shearing—this results in significant dilation when subject to an increased sliding velocity and an enhancement in permeability. Such fractures are likely frictionally unstable to neutral [*Niemeijer and Spiers*, 2007], which means that the induced fault slip is on the boundary between seismic slip and aseismic slip. (2) The fracture comprises weak-brittle minerals are relatively easier to be crushed into small particles. When the shearing rate increases, the generated wear products initiate dilation but then continue to comminute into finer particles that are subsequently compacted during shearing. These types of fractures tend to be frictionally neutral to stable. (3) The fracture material is weak ductile and clay rich, with velocity-strengthening property and dominated by swelling caused by fluid infiltration. While fluid passes through the fracture, the swelling clays close the aperture. Concurrently, the shearing process comminutes the swelling fracture asperities into fine particles and distorts particles, resulting in the formation of fabric layer—thin clay-rich foliae, along which the frictional strength is reduced but the stability is increased and the fluid pathway is fully sealed. When the permeability is significantly reduced to its steady state, a change in shearing velocity does not change the permeability. This conceptual model, although not supported by an exhaustive suite of experimental observations on all natural shale rocks, is consistent with the experiments reported here and with the grain packing framework model from previous experimental studies on shales and other sedimentary rocks [*Crawford et al.*, 2008; *Tembe et al.*, 2010; *Kohli and Zoback*, 2013]. Additionally, there are other factors influencing frictional stability, such as fluid pressure, temperature, sliding velocity and presence of carbonate-rich material content [*Niemeijer and Collettini*, 2013; *Verberne et al.*, 2014], while in this study, keeping these potential influencing factors constant will help us better capture fundamental features of the frictional stability-permeability relationship under the simplest variation (i.e., mineralogy). Integrated effects with multiple influencing factors are worth investigating in the further work.
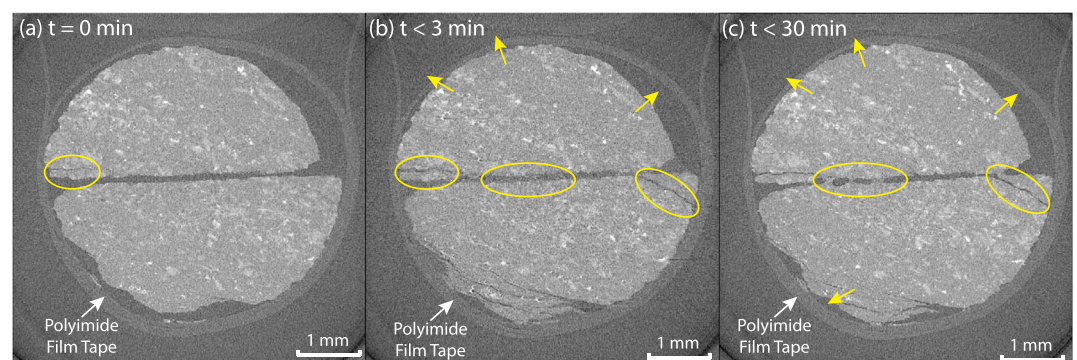
Figure 12. xCT images of Opalinus shale fracture under wetting conditions without confining pressure. (a) Dry Opalinus shale fracture. (b) Wet Opalinus shale fracture 3 min after wetting. (c) Wet Opalinus shale fracture 30 min after wetting when water drop is fully evaporated. The yellow arrows point the swelling expansion direction. The highlighted circles points out where swelling occurring on fracture surfaces.
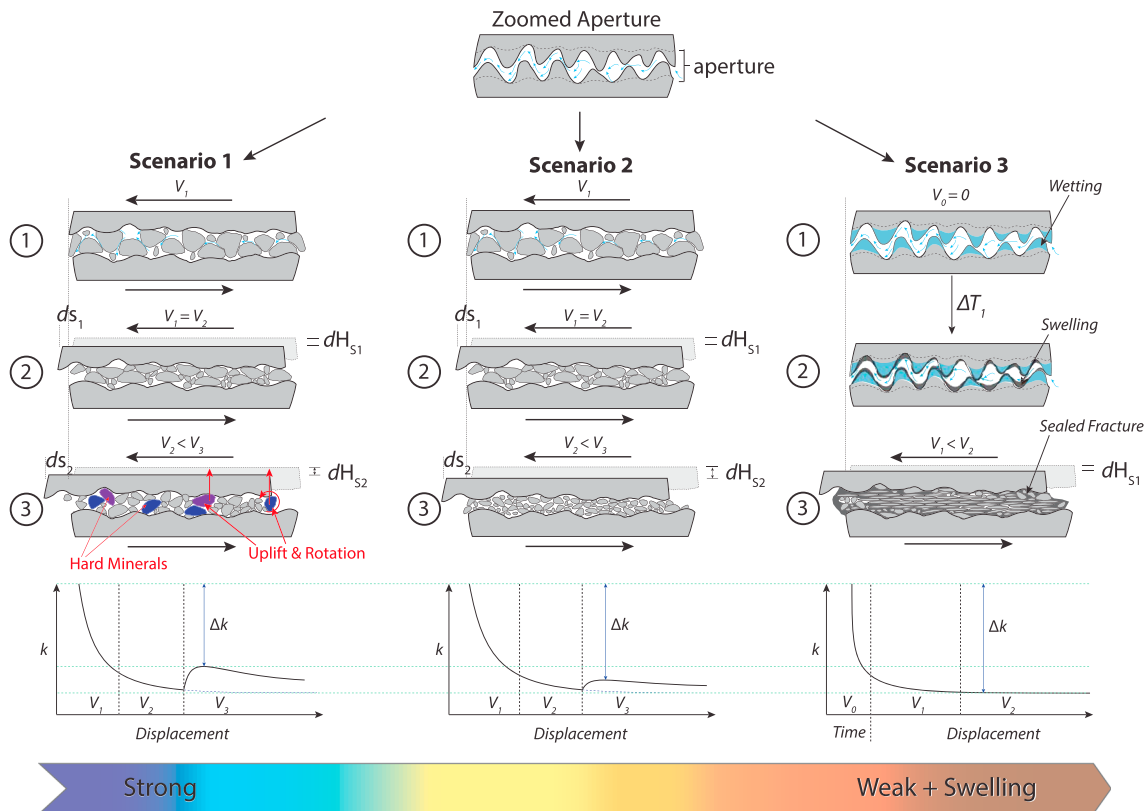
Figure 13. Conceptual model of asperity and permeability evolution of planar saw cut fractures. Scenario 1: End-member of clay-poor, brittle-like fracture material that is composed of hard minerals. During the shearing, the hard minerals are difficult to comminute into small particles and the fracture may dilate significantly. Scenario 2: Intermediate case between clay-poor and clay-rich end-member. The fracture material is brittle and comprises weak minerals that are easier to be crushed into fine particles and compacted with shear displacement. Scenario 3: End-member of clay-rich and weak-ductile fracture material that is composed of soft minerals. When subject to shearing, the soft minerals readily deform and comminute into smaller particles and fill the trough. With effect of fluid infiltration, clay swelling leads to a thin layer of clay-rich foliae that seals the fracture.

4. Conclusion

In order to understand the mode of fracture reactivation and permeability evolution in shales in a low effective normal stress regime, we performed direct-shearing experiment to measure the frictional strength and stability while also measuring permeability changes. We find that under low effective normal stress, phyllosilicate-rich shale (OPS) exhibits weaker frictional strength but much stronger frictional stability and larger permeability reduction than that of carbonate-rich shale (GRS). Our experimental and analytical results show that this observed friction-stability-permeability relationship may be explained via an integration of three interconnected physical mechanisms: (1) different mineral composition of fractures has a distinct effect on frictional strength and frictional stability. At low effective normal stress, phyllosilicate-rich OPS tends to be more frictionally stable than that of carbonate-rich GRS. (2) Generated wear products of low surface roughness fractures would seal the fluid conduits of fracture aperture, countering the effect of fracture dilation. The competition between wear product and fracture dilation depends on material strength and brittleness —strong-brittle asperities may result in higher frictional strength, lower frictional stability, and larger permeability than that of weak-ductile asperities. (3) Swelling of clay-rich asperities and clay-rich wear products directly seals the fracture aperture and therefore reduces the permeability. This relationship implies that a comprehensive mineralogical characterization of reservoir rock and fractures may help in a preliminary understanding of potential permeability evolution subject to fluid injection in shale rocks. In the context of shale reservoir site selection, we speculate that shallow depth overpressure may induce aseismic events in clay-rich shales causing low roughness fractures to seal and secure the integrity of shale reservoir.

References

Allis, R. G., T. C. Chidsey, W. Gwynn, C. Morgan, S. White, M. Adams, and J. Moore (2001), Natural CO_2 reservoirs on the Colorado plateau and southern Rocky Mountains: Candidates for CO_2 sequestration, paper presented at the 1st Annual Conference on Carbon and Sequestration, U.S. DOE/NETL, Alexandria, Va.

Amorim, C. L. G., R. T. Lopes, R. C. Barroso, J. C. Queiroz, D. B. Alves, C. A. Perez, and H. R. Schelin (2007), Effect of clay–water interactions on clay swelling by X-ray diffraction, *Nucl. Instruments Methods Phys. Res. Sect. A Accel. Spectrometers, Detect. Assoc. Equip.*, *580*, 768–770, doi:10.1016/j.nima.2007.05.103.

Anderson, J. G., S. G. Wesnousky, and M. W. Stirling (1996), Earthquake size as a function of fault slip rate, *Bull. Seismol. Soc. Am.*, *86*, 683–690.

Anderson, R. N., and M. D. Zoback (1982), Permeability, underpressures, and convection in the oceanic crust near the Costa Rica Rift, eastern equatorial Pacific, *J. Geophys. Res.*, *87*, 2860–2868, 10.1029/JB087iB04p02860.

Barton, N., S. Bandis, and K. Bakhtar (1985), Strength, deformation and conductivity coupling of rock joints, *Int. J. Rock Mech. Min. Sci.*, *22*(3), 121–140, doi:10.1016/0148-9062(85)93227-9.

Bossart, P., T. Trick, P. M. Meier, and J.-C. Mayor (2004), Structural and hydrogeological characterisation of the excavation-disturbed zone in the Opalinus Clay (Mont Terri Project, Switzerland), *Appl. Clay Sci.*, *26*, 429–448.

Bredehoeft, J. D. R. G. Wolff, W. S. Keys, and E. Shuter (1976), Hydraulic fracturing to determine the regional in situ stress field, Piceance Basin, Colorado, *Geol. Soc. Am. Bull.*, *87*, 250–258, doi:10.1130/0016-7606(1976)87<250:HFTDTR>2.0.CO;2.

Brown, S. R., and C. H. Scholz (1985), Broad bandwidth study of the topography of natural rock surfaces, *J. Geophys. Res.*, *90*(B14), 12,575, doi:10.1029/JB090iB14p12575.

Brune, J. N. (1968), Seismic moment, seismicity, and rate of slip along major fault zones, *J. Geophys. Res.*, *73*(2), 777, doi:10.1029/JB073i002p00777.

Corkum, A. G., and C. D. Martin (2007), Modelling a mine-by test at the Mont Terri rock laboratory, Switzerland, *Int. J. Rock Mech. Min. Sci.*, *44*, 846–859, doi:10.1016/j.ijrmms.2006.12.003.

Crawford, B. R., D. R. Faulkner, and E. H. Rutter (2008), Strength, porosity, and permeability development during hydrostatic and shear loading of synthetic quartz-clay fault gouge, *J. Geophys. Res.*, *113*, 1–14, doi:10.1029/2006JB004634.

Davies, J. P., and D. K. Davies (2001), Stress-dependent permeability: Characterization and modeling, *Soc. Pet. Eng. J.*, *6*(2), 224–235, doi:10.2118/71750-PA.

Dieterich, J. H. (1978), Time-dependent friction and the mechanics of stick-slip, *Pure Appl. Geophys. PAGEOPH*, *116*, 790–806, doi:10.1007/BF00876539.

Dieterich, J. H. (1979), Modeling of rock friction: 1. Experimental results and constitutive equations, *J. Geophys. Res.*, *84*, 2161–2168, doi:10.1029/JB084iB05p02161.

Dieterich, J. H. (1992), Earthquake nucleation on faults with rate-and state-dependent strength, *Tectonophysics*, *211*(1–4), 115–134, doi:10.1016/0040-1951(92)90055-B.

Dodd, C. G., F. R. Conley, and P. M. Barnes (1955), Clay minerals in petroleum reservoir sands and water sensitivity effects, *Clays Clay Miner*, *3*, 221–238.

Dyni, J. R. (2006), *Geology and Resources of Some World Oil-Shale Deposits*, US Department of The Interior, US Geological Survey.

Ellsworth, W. L. (2013), Injection-induced earthquakes, *Science*, *341*, 142–149, doi:10.1126/science.1225942.

Elsworth, D., and R. E. Goodman (1986), Characterization of rock fissure hydraulic conductivity using idealized wall roughness profiles, *Int. J. Rock Mech. Min. Sci. Geomech. Abstr.*, *23*(3), 233–243, doi:10.1016/0148-9062(86)90969-1.

Fang, Y., S. A. M. den Hartog, D. Elsworth, C. Marone, and T. Cladouhos (2016), Anomalous distribution of microearthquakes in the Newberry Geothermal Reservoir: Mechanisms and implications, *Geothermics*, *63*, 62–73, doi:10.1016/j.geothermics.2015.04.005.

Faoro, I., A. Niemeijer, C. Marone, and D. Elsworth (2009), Influence of shear and deviatoric stress on the evolution of permeability in fractured rock, *J. Geophys. Res.*, *114*(1), doi:10.1029/2007JB005372.

Gualda, G. A. R., and M. Rivers (2006), Quantitative 3D petrography using X-ray tomography: Application to Bishop Tuff pumice clasts, *J. Volcanol. Geoth. Res.*, *154*(1–2), 48–62, doi:10.1016/j.jvolgeores.2005.09.019.

Guglielmi, Y., F. Cappa, J.-P. Avouac, P. Henry, and D. Elsworth (2015), Seismicity triggered by fluid injection–induced aseismic slip, *Science*, *348*, 1224–1226, doi:10.1126/science.aab0476.

Healy, J. H., W. W. Rubey, D. T. Griggs, and C. B. Raleigh (1968), The Denver earthquakes, *Science*, *161*(3848), 1301–1310, doi:10.1126/science.161.3848.1301.

Heidug, W. K., and S. Wong (1996), Hydration swelling of water-absorbing rocks: A constitutive model, *Int. J. Numer. Anal. methods Geomech.*, *20*(6), 403–430.

Ikari, M. J., C. Marone, and D. M. Saffer (2011), On the relation between fault strength and frictional stability, *Geology*, *39*, 83–86, doi:10.1130/g31416.1.

Ishibashi, T., N. Watanabe, H. Asanuma, and N. Tsuchiya (2016), Linking microearthquakes to fracture permeability change: The role of surface roughness, *Geophys. Res. Lett.*, *43*, 7486–7493, doi:10.1002/2016GL069478.

Kanamori, H., and E. Hauksson (1992), A slow earthquake in the Santa Maria Basin, *Bull. Seismol. Soc. Am.*, *82*(5), 2087–2096.

Kaufhold, A., W. Gräsle, I. Plischke, R. Dohrmann, and S. Siegesmund (2013), Influence of carbonate content and micro fabrics on the failure strength of the sandy facies of the Opalinus Clay from Mont Terri (Underground Rock Laboratory), *Eng. Geol.*, *156*, 111–118, doi:10.1016/j.enggeo.2013.01.014.

Kohli, A. H., and M. D. Zoback (2013), Frictional properties of shale reservoir rocks, *J. Geophys. Res. Solid Earth*, *118*, 5109–5125, doi:10.1002/jgrb.50346.

Majer, E. L., R. Baria, M. Stark, S. Oates, J. Bommer, B. Smith, and H. Asanuma (2007), Induced seismicity associated with Enhanced Geothermal Systems, *Geothermics*, *36*, 185–222, doi:10.1016/j.geothermics.2007.03.003.

Marone, C. (1997), On the rate of frictional healing and the constitutive law for time- and slip-dependent friction, *Int. J. Rock Mech. Min. Sci. Geomech. Abstr.*, *34*, 347, doi:10.1016/S1365-1609(97)00054-3.

Marone, C. (1998), Laboratory-derived friction laws and their application to seismic faulting, *Annu. Rev. Earth Planet. Sci.*, *26*, 643–696, doi:10.1146/Annurev.Earth.26.1.643.

Mazumder, S., and K. H. Wolf (2008), Differential swelling and permeability change of coal in response to CO_2 injection for ECBM, *Int. J. Coal Geol.*, *74*, 123–138.

McGarr, A., D. Simpson, and L. Seeber (2002), 40 Case histories of induced and triggered seismicity, *Int. Geophys.*, *81*(PART A), 647–661, doi:10.1016/S0074-6142(02)80243-1.

Misra, A. (2002), Effect of asperity damage on shear behavior of single fracture, *Eng. Fract. Mech.*, *69*(17), 1997–2014, doi:10.1016/S0013-7944 (02)00073-5.

Mohan, K. K., R. N. Vaidya, M. G. Reed, and H. S. Fogler (1993), Water sensitivity of sandstones containing swelling and non-swelling clays, *Colloids Surf., A*, *73*, 237–254, doi:10.1016/0927-7757(93)80019-B.

Niemeijer, A., and C. Collettini (2013), Frictional properties of a low-angle normal fault under in situ conditions: Thermally-activated velocity weakening, *Pure Appl. Geophys.*, 1–24, doi:10.1007/s00024-013-0759-6.

Niemeijer, A. R., and C. J. Spiers (2007), A microphysical model for strong velocity weakening in phyllosilicate-bearing fault gouges, *J. Geophys. Res.*, *112*, B10405, doi:10.1029/2007JB005008.

Norrish, K. (1954), The swelling of montmorillonite, *Discuss. Faraday Soc.*, *18*(0), 120–134, doi:10.1039/DF9541800120.

Norrish, K., and J. P. Quirk (1954), Crystalline swelling of montmorillonite: Use of electrolytes to control swelling, *Nature*, *173*(4397), 255–256.

Peng, Z., and J. Gomberg (2010), An integrated perspective of the continuum between earthquakes and slow-slip phenomena, *Nat. Geosci.*, *3*, 599–607, doi:10.1038/ngeo940.

Rabinowicz, E. (1951), The nature of the static and kinetic coefficients of friction, *J. Appl. Phys.*, *22*(1951), 1373–1379, doi:10.1063/1.1699869.

Raleigh, C. B., J. H. Healy, and J. D. Bredehoeft (1976), An experiment in earthquake control at Rangely, Colorado, *Science*, *191*(4233), 1230–1237, doi:10.1126/science.191.4233.1230.

Rice, J. R. (2006), Heating and weakening of faults during earthquake slip, *J. Geophys. Res.*, *111*, 1–29, doi:10.1029/2005JB004006.

Ruina, A. (1983), Slip instability and state variable friction laws, *J. Geophys. Res.*, *88*(B12), 10,359–10,370, doi:10.1029/JB088iB12p10359.

Rutqvist, J., Y.-S. Wu, C.-F. Tsang, and G. Bodvarsson (2002), A modeling approach for analysis of coupled multiphase fluid flow, heat transfer, and deformation in fractured porous rock, *Int. J. Rock Mech. Min. Sci.*, *39*(4), 429–442, doi:10.1016/S1365-1609(02)00022-9.

Rutqvist, J., C. F. Tsang, and Y. Tsang (2004), Analysis of stress and moisture induced changes in fractured rock permeability at the yucca mountain drift scale test, in *Elsevier Geo-Engineering Book Series*, vol. 2, edited by S. Ove, pp. 161–166, Elsevier.

Samuelson, J., D. Elsworth, and C. Marone (2009), Shear-induced dilatancy of fluid-saturated faults: Experiment and theory, *J. Geophys. Res.*, *114*, 1–15, doi:10.1029/2008JB006273.

Schmidt, D. A., R. Bürgmann, R. M. Nadeau, and M. D'Alessio (2005), Distribution of aseismic slip rate on the Hayward fault inferred from seismic and geodetic data, *J. Geophys. Res.*, *110*, 1–15, doi:10.1029/2004JB003397.

Scholz, C. H. (1998), Earthquakes and friction laws, *Nature*, *391*(6662), 37–42, doi:10.1038/34097.

Shapiro, S. A., C. Dinske, and E. Rothert (2006), Hydraulic-fracturing controlled dynamics of microseismic clouds, *Geophys. Res. Lett.*, *33*, doi:10.1029/2006GL026365.

Snow, D. T. (1969), Anisotropic permeability of fractured media, *Water Resour. Res.*, *5*(6), 1273–1289, doi:10.1029/WR005i006p01273.

Suckale, J. (2009), Induced seismicity in hydrocarbon fields, *Adv. Geophys.*, *51*, 1976–1984, doi:10.1016/S0065-2687(09)05107-3.

Tanikawa, W., M. Sakaguchi, O. Tadai, and T. Hirose (2010), Influence of fault slip rate on shear-induced permeability, *J. Geophys. Res.*, *115*, 1–18, doi:10.1029/2009JB007013.

Tanikawa, W., O. Tadai, and H. Mukoyoshi (2014), Permeability changes in simulated granite faults during and after frictional sliding, *Geofluids*, *14*, 481–494, doi:10.1111/gfl.12091.

Tembe, S., D. A. Lockner, and T. F. Wong (2010), Effect of clay content and mineralogy on frictional sliding behavior of simulated gouges: Binary and ternary mixtures of quartz, illite, and montmorillonite, *J. Geophys. Res.*, *115*, doi:10.1029/2009JB006383.

Verberne, B. A., C. J. Spiers, A. R. Niemeijer, J. H. P. De Bresser, D. A. M. De Winter, and O. Plümper (2014), Frictional properties and microstructure of calcite-rich fault gouges sheared at sub-seismic sliding velocities, *Pure Appl. Geophys.*, *171*, 2617–2640, doi:10.1007/s00024-013-0760-0.

Walsh, F. R., and M. D. Zoback (2015), Oklahoma's recent earthquakes and saltwater disposal, *Sci. Adv.*, *1*(5), 1–9.

Wang, W., and C. H. Scholz (1994), Wear processes during frictional sliding of rock: A theoretical and experimental study, *J. Geophys. Res.*, *99*(B4), 6789–6799, doi:10.1029/93JB02875.

Wenk, H. R., M. Voltolini, M. Mazurek, L. R. Van Loon, and A. Vinsot (2008), Preferred orientations and anisotropy in shales: Callovo-oxfordian shale (France) and opalinus clay (Switzerland), *Clays Clay Miner.*, *56*, 285–306, doi:10.1346/CCMN.2008.0560301.

Xu, T., and K. Pruess (2004), Numerical simulation of injectivity effects of mineral scaling and clay swelling in a fractured geothermal reservoir, Lawrence Berkeley Natl Lab., Berkeley, Calif.

Yasuhara, H., D. Elsworth, and A. Polak (2004), Evolution of permeability in a natural fracture: Significant role of pressure solution, *J. Geophys. Res.*, *109*, doi:10.1029/2003JB002663.

Yasuhara, H., A. Polak, Y. Mitani, A. S. Grader, P. M. Halleck, and D. Elsworth (2006), Evolution of fracture permeability through fluid-rock reaction under hydrothermal conditions, *Earth Planet. Sci. Lett.*, *244*, 186–200, doi:10.1016/j.epsl.2006.01.046.

Yoshioka, N. (1997), A review of the micromechanical approach to the physics of contacting surfaces, *Tectonophysics*, *277*(1–3), 29–40, doi:10.1016/S0040-1951(97)00076-0.

Yoshioka, N., and C. H. Scholz (1989), Elastic properties of contacting surfaces under normal and shear loads: 2. Comparison of theory with experiment, *J. Geophys. Res.*, *94*, 17,691, doi:10.1029/JB094iB12p17691.

Young, D. A., and D. E. Smith (2000), Simulations of clay mineral swelling and hydration: Dependence upon interlayer ion size and charge, *J. Phys. Chem. B.*, *104*(39), 9163–9170.

Zhong, Z., D. Elsworth, and Y. Hu (2016), Evolution of strength and permeability in stressed fractures with fluid–rock interactions, *Pure Appl. Geophys.*, *173*(2), 525–536.

Zoback, M. D., and S. M. Gorelick (2012), Reply to Juanes et al.: Evidence that earthquake triggering could render long-term carbon storage unsuccessful in many regions, *Proc. Natl. Acad. Sci. U.S.A.*, *109*, E3624–E3624, doi:10.1073/Pnas.1217264109.